



ELSEVIER

Contents lists available at ScienceDirect

Journal of Magnetism and Magnetic Materials

journal homepage: www.elsevier.com/locate/jmmm

Research articles

Antiferromagnetism of the cation-ordered warwickite system $Mn_{2-x}Mg_xBO_4$ ($x = 0.5, 0.6$ and 0.7)

N.V. Kazak^{a,*}, N.A. Belskaya^b, E.M. Moshkina^a, L.N. Bezmaternykh^a, A.D. Vasiliev^{a,c},
S.N. Sofronova^a, R.M. Eremina^{d,e}, E.V. Eremin^{a,c}, A.R. Muftakhutdinov^e, M.A. Cherosov^e,
S.G. Ovchinnikov^{a,c}

^a Kirensky Institute of Physics, FRC SB RAS, Krasnoyarsk, Russia^b Reshetnev Siberian State University of Science and Technology, Krasnoyarsk, Russia^c Siberian Federal University, Krasnoyarsk, Russia^d Zavoisky Physical-Technical Institute, FRC Kazan Scientific Centre of RAS, Kazan, Russia^e Kazan (Volga Region) Federal University, Kazan, Russia

ARTICLE INFO

Keywords:

Warwickites
Antiferromagnet
Cation ordering
Jahn-Teller distortions

ABSTRACT

X-ray diffraction, heat capacity and magnetic measurements are performed on single crystals of $Mn_{2-x}Mg_xBO_4$ ($x = 0.5, 0.6$ and 0.7) with the warwickite structure. The monoclinic symmetry is found for all samples with the space group $P2_1/n$. The M1 site is occupied by trivalent Mn ions while the M2 site is occupied by a mixture of divalent Mg and Mn ions. Regular cation and charge distributions are observed, which is unusual for heterometallic warwickites. The local octahedral distortions of $M1O_6$ show the monotonic dependence on the Mg content and are in accordance with the Jahn-Teller distortion. All samples are found to undergo long-range antiferromagnetic ordering with rather low transition temperatures of $T_N = 16, 14$ and 13 K for $x = 0.5, 0.6$, and 0.7 , respectively. The ordering of local octahedral distortions, caused by the strong electron-phonon interaction of the trivalent Mn ions, is proposed to stabilise the cationic ordering and, as a result, the long-range magnetic ordering in the material.

1. Introduction

Transition-metal oxyborates represent a common mineral class. These minerals are formed at all stages of geological processes, which is the reason for the significant interest in these systems from geophysical and geochemical points of view. For example, the isomorphous pair of $2Fe^{3+} \cdot (Mg^{2+} + Ti^{4+})$ forms a continuous row of solid solutions of rock-forming minerals: Mg_2FeBO_5 ludwigite – Fe_3BO_5 vonsenite [1], $Mg_{1.5}Ti_{0.5}BO_4$ warwickite – $MgFeBO_4$ yuanfuliite [2]. Moreover, these materials are also of interest with regards to fundamental physics. The strong relationship between the spin, orbital and lattice degrees of freedom allows for observations of a variety of cooperative phenomena, including charge and orbital ordering, cascades of magnetic phase transitions, structural transformations accompanied by conductivity anomalies and charge density waves formation [3–10]. A number of studies have demonstrated the potential of borates as high capacity cathode materials for Li and Na batteries [11–13].

Recently, a significant attention has been devoted to complex oxyborates that are isostructural to ludwigite and warwickite minerals

[14–16]. The general formula of these compounds is $M^{2+}_nM^{3+}_nO_nBO_3$, where $n = 1$ for the warwickites and $n = 2$ for the ludwigites. Metallic ions occupy $2n$ crystallographic non-equivalent positions and have octahedral oxygen coordination (Fig. 1). A notable peculiarity of these materials is the tendency of the di- and trivalent ions to form ordered planes parallel to the short crystallographic direction (a crystal parameter of $c = \sim 3$ Å). The ratio of di- and trivalent ions per formula unit determines the ability of the system to form the ordered planes. Therefore, in the ludwigites, where $M^{2+}/(B^{3+}, M^{3+}) = 1:1$, the divalent ions filling the 1, 2 and 3 metal sites build the planes spatially separated by the planes of trivalent ions (boron and M^{3+} ions at site 4). Warwickites, where this ratio is 1:2, are prone to forming mixed cation planes.

The distribution of the di- and trivalent cations over distinct metal sites determines the oxidation states at a particular site and, ultimately, the magnetic ground state. Thus, the ludwigites tend to exhibit long-range order. For example, $M_2^{2+}Fe^{3+}BO_5$ ($M^{2+} = Fe$ or Co) shows cascade magnetic transitions associated with the magnetic ordering of two spin ladders (3-1-3 and 4-2-4) at Neel temperatures $T_{N1} = 112$ K

* Corresponding author at: Laboratory of Physics of Magnetic Phenomena, Kirensky Institute of Physics, Akademgorodok 50, bld. 38, Krasnoyarsk 660036, Russia.
E-mail address: nat@iph.krasn.ru (N.V. Kazak).

<https://doi.org/10.1016/j.jmmm.2020.166820>

Received 7 February 2020; Received in revised form 13 March 2020; Accepted 26 March 2020

Available online 27 March 2020

0304-8853/© 2020 Elsevier B.V. All rights reserved.

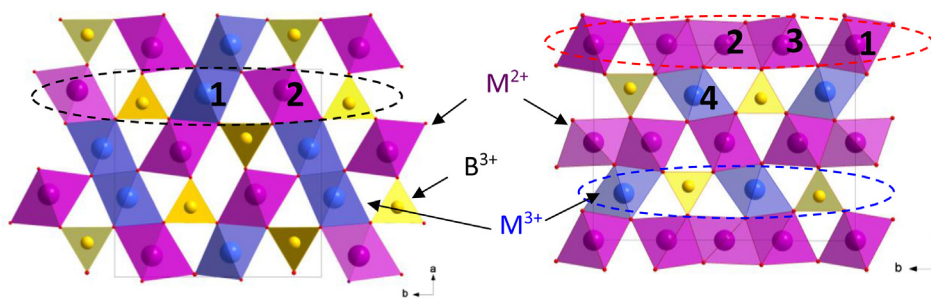


Fig. 1. Crystal structures of M_2BO_4 (left, $Pnam$ (No.62)) and M_3BO_5 (right, $Pbam$ (No.55)) with warwickite and ludwigite structures, respectively. The edge-sharing octahedra occupied by M^{2+} and M^{3+} ions are highlighted by pink and blue, respectively. The distinct crystallographic sites are numbered. The B^{3+} ions are at the centre of the trigonal BO_3 groups (yellow triangles). Dashed lines show the different types of cation planes: space-separated planes of di- and trivalent ions in the ludwigite structure and valence-mixed planes in the warwickite structure. (For interpretation of the references to colour in this figure legend, the reader is referred to the web version of this article.)

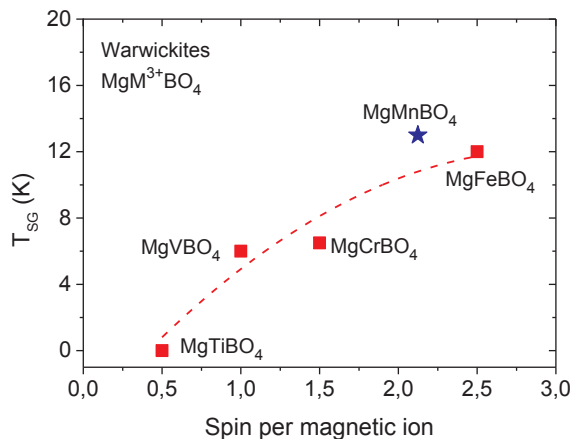


Fig. 2. Temperatures of magnetic transitions as a function of spin value in the magnesium warwickites $MgMBO_4$ ($M = Ti^{3+}, V^{3+}, Cr^{3+}, Mn^{3+}$ or Fe^{3+}). The $MgMnBO_4$ warwickite only undergoes the antiferromagnetic transition while other materials show spin-glass transitions. The dashed line is a guide for the eye.

(PM-AFM) and $T_{N2} = 74$ K (AFM-Ferri), respectively [4,5]. In Co_3BO_5 , the Co^{3+} ions exclusively filling the M4 site are in the low-spin state (d^6 , $S = 0$) that makes this oxyborate a ferrimagnet with $T_N = 42$ K [5,6].

Unlike ludwigites, warwickites show a much stronger tendency for cationic disorder and are classified as intrinsically disordered systems. The numerous heterometallic warwickites are magnetically disordered systems. They undergo the transition to the spin-glass state with the intermediate temperature phase – random exchange Heisenberg antiferromagnetic chains [8,9,17,18] or demonstrate the properties of the random singlet phase [19]. The effects of the magnetic frustrations arising from the cation disorder and the crystal structure peculiarities are manifested in the extremely high parameter of magnetic frustration $\eta = \frac{\rho}{T_{SG}} > 10$ [9,17]. In contrast, homometallic warwickites demonstrate a long-range order. So far, only three of six hypothetically possible homometallic warwickites ($M^{2+} = M^{3+} = Ti, V, Cr, Mn, Fe$ or Co) have been synthesised, namely, Mn_2BO_4 [20,21], Fe_2BO_4 [22] and V_2BO_4 [23]. All of them demonstrate cationic and charge orderings. The transition to the charge ordering phase is accompanied by the orthorhombic \rightarrow monoclinic symmetry lowering. This suggests that the long-range magnetic order in the warwickites is determined by the cation order and as a consequence by the charge state at the particular metal site. If so, then the following questions arise: i) is it possible to achieve long-range magnetic order in the heterometallic warwickites?; ii) how can the cation order in these systems be reached?

As an initial focus, the Mn_2BO_4 homometallic system has been chosen. In this system, the charge ordering is a consequence of the dz^2 -orbital order. Recent experiments using high-temperature powder

diffraction have shown that the local octahedral distortions around the Jahn-Teller ions (M1 sites) are conserved up to 800 K, as well as the orderliness of the arrangement of these octahedra. The elongated axial Mn1-O bond lengths are stacked in double chains, leading to the ordering of strains and a periodicity of charge distribution. The Mn^{3+} electron lattice is expected to be strongly pinned on a crystal lattice. This leads to a gain in the electrostatic energy in the case of the Mn^{3+} ions located at “preferred” M1 sites. Therefore, Mn_2BO_4 , allowing both di- and trivalent substitution, is a good model system with which one can trace the long-range order origination.

Recently, the heterometallic warwickite system $Mn_{2-x}Fe_xBO_4$ ($x = 0.3, 0.5$ and 0.7) has been comprehensively studied using X-ray diffraction, X-ray absorption (XANES/EXAFS), Mössbauer spectroscopy, heat capacity and magnetic measurements [24,25]. The orthorhombic structure ($Pnam$) is found for all samples. The substitution of Mn^{3+} ions for Fe^{3+} ions with close ionic radii, $r_i(Mn^{3+}) = r_i(Fe^{3+}) = 0.645$ Å according to Shannon [26], induces the breakage of the long-range magnetic order and the onset of the short-range order AF correlations, which are enhanced with increasing Fe content. As a result, the spin-glass transition was observed below $T_{SG} = 11$ –17 K, depending on the Fe concentration. Mössbauer spectroscopy measurements have shown that the Fe^{3+} ions in the high-spin state are distributed over two metal sites, thereby causing cation disorder. Here, we focus on the $Mn_{1-x}Mg^{2+}_xMn^{3+}_xBO_4$ ($0.0 < x < 1.0$) warwickites, where the Jahn-Teller ions are preserved.

There are several known magnesium-based warwickites, including $MgTiBO_4$ [19], $MgVBO_4$ [9], $MgCrBO_4$ [9] and $MgFeBO_4$ [9,17,18], which show the transition to the spin-glass state at low temperatures. As seen from Fig. 2, the critical temperature monotonically increases with the spin value of the magnetic ion increasing. The $Mg_{0.76}Mn_{1.24}BO_4$ compound has already been reported by Norrestam [27], but its physical properties were hitherto unknown. Our recent work has revealed that the Mg-Mn warwickite system shows signs of the antiferromagnetic long range order below $T_N = 16$ K [28]. The present study investigates the effect of the divalent substitution Mn^{2+} - Mg^{2+} on the cation order, the charge states of the metal sites, the local octahedral distortions and the magnetic properties of $Mn_{2-x}Mg_xBO_4$ ($0.0 < x < 1.0$) solid solutions.

2. Experimental methods

Single crystals of $Mn_{2-x}Mg_xBO_4$ solid solutions were obtained using flux synthesis from the system $(100 - n)\%mass(Bi_2Mo_3O_{12} + pB_2O_3 + qNa_2O)$. The magnesium oxide content (x), q and p coefficients and concentration n are shown in Table 1. The fluxes for each x and the corresponding parameters of the flux system were prepared in a platinum crucible ($V = 100$ cm³) at a temperature of 1100 °C by sequential melting of powder mixtures: first, $Bi_2Mo_3O_{12}$ and B_2O_3 , then Mn_2O_3 and MgO , and finally, the powder of Na_2CO_3 added in portions. The high-temperature crystallising phase in

Table 1

Parameters of fluxes: magnesium concentration (x), crystal-forming oxide concentration (n), weight coefficients – concentration of the boron and sodium oxides (p and q , respectively) and saturation temperatures (T_{sat}).

x	0.5	0.6	0.7
n , %	19.0	20.0	20.9
p	1.90	1.82	1.73
q	1.40	1.75	2.10
T_{sat} , °C	845	870	880

a sufficiently wide temperature range (no less than 40 °C) was the $Mn_{2-x}Mg_xBO_4$ warwickite phase. The saturation temperatures of fluxes depending on the concentration x are presented in Table 1.

After the preparation process, the fluxes were homogenised at 1100 °C for 3 h. When the homogenisation is completed, the platinum crystal holder (rod) was inserted to the flux. Then, the temperature was first rapidly reduced to $T_{sat}-10$ °C and then slowly reduced at a rate of 4 °C/day. In five days, the growth was completed, the crystal holder with single crystals was extracted from the flux. Grown single crystals, in a shape of black prisms in a length up to 5 mm and the cross-section size up to 0.4×0.4 mm², were separated from the crystal holder and flux remainder by etching in a 20% solution of nitric acid. Single crystals of $Mn_{2-x}Mg_xBO_4$ with $x = 0.5, 0.6$ and 0.7 were obtained.

An X-ray crystallographic study was carried out with a SMART APEX II single crystal diffractometer (Bruker AXS) equipped with a PHOTON 2 CCD detector, graphite monochromator and Mo K α radiation source. The X-ray diffraction experiments were performed in Krasnoyarsk Regional Center of Research Equipment of Federal Research Center «Krasnoyarsk Science Center SB RAS». The structure was solved by direct methods [29] using the SHELXS program. The structural refinement was carried out by least-square minimisation in the SHELXL program [30] using anisotropic thermal parameters of all atoms. The main information regarding crystal data, data collection and refinement is reported in Table SM1 [31].

The dc magnetisation measurements were performed on single crystals using a Quantum Design PPMS in the temperature range of 2–300 K and an external magnetic field of 10 kOe. The magnetic field was applied parallel and perpendicular to the needle axis, which coincides with the c axis of the crystal. For the $Mn_{1.4}Mg_{0.6}BO_4$ composition, the magnetic measurements were carried out at low temperatures and high magnetic fields (± 90 kOe) in Krasnoyarsk Regional Center of Research Equipment of Federal Research Center «Krasnoyarsk Science Center SB RAS».

The heat capacity as a function of temperature was measured on single crystals using the Quantum Design PPMS. The crystals were glued to the sample holder with Apiezon grease.

3. Results

3.1. Crystal structure

The symmetry and space group were found to be monoclinic and $P2_1/n$ (No. 14), respectively, for all samples. With the MgO concentration increase, the solid solutions were found to crystallise in the hulsite ($P2_1/m$ (No.10)) [32] and orthopinakiolite (Pbam (No.55)) [33] structures with general formula $Mn_{3-x}Mg_xBO_5$. The atom coordinates, thermal parameters and selected interionic distances are listed in Tables SM2–SM4 [31], respectively.

It is noteworthy that the Mg-Mn system under investigation shows cation ordering, where the Mg atoms have an evident tendency to occupy the M2 site. The magnesium atom distribution is almost independent of the Mg concentration and can be determined as Mg(1):Mg(2) = 0.1:0.9 (Fig. 3). We conclude that the isovalent substitution $Mn^{2+} \rightarrow Mg^{2+}$ does not induce remarkable cationic disorder as established for other heterometallic warwickites.

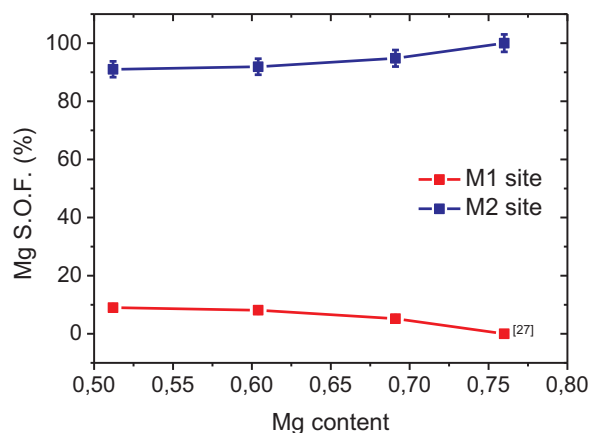


Fig. 3. Magnesium site occupation factor (S.O.F.) as a function of Mg content in $Mn_{2-x}Mg_xBO_4$ solid solutions, where the Mg content is extracted from XRD data. The data for $x = 0.76$ are taken from the original work [27].

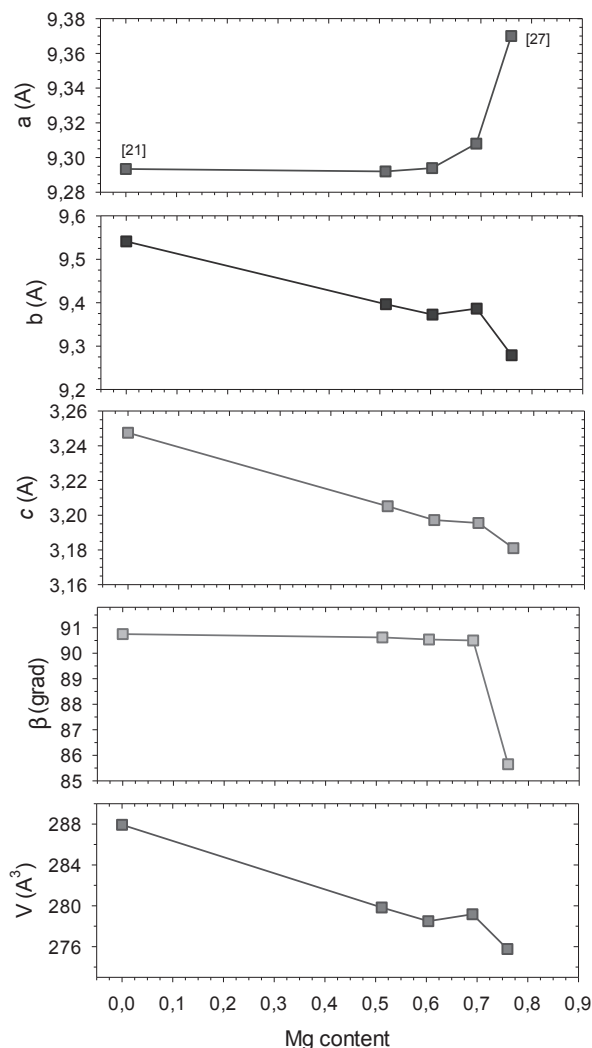


Fig. 4. Lattice parameters and volume of $Mn_{2-x}Mg_xBO_4$ solid solutions with varying Mg content. The errors are smaller than the symbol size. Hereinafter, we use the crystal data for $x = 0.0$ and 0.76 obtained from Refs. [21] and [27], respectively.

Fig. 4 shows the dependencies of the lattice parameters of the $Mn_{2-x}Mg_xBO_4$ solid solutions versus the Mg concentration along with the data for Mn_2BO_4 [21] and $Mn_{1.24}Mg_{0.76}BO_4$ [27]. One can see that

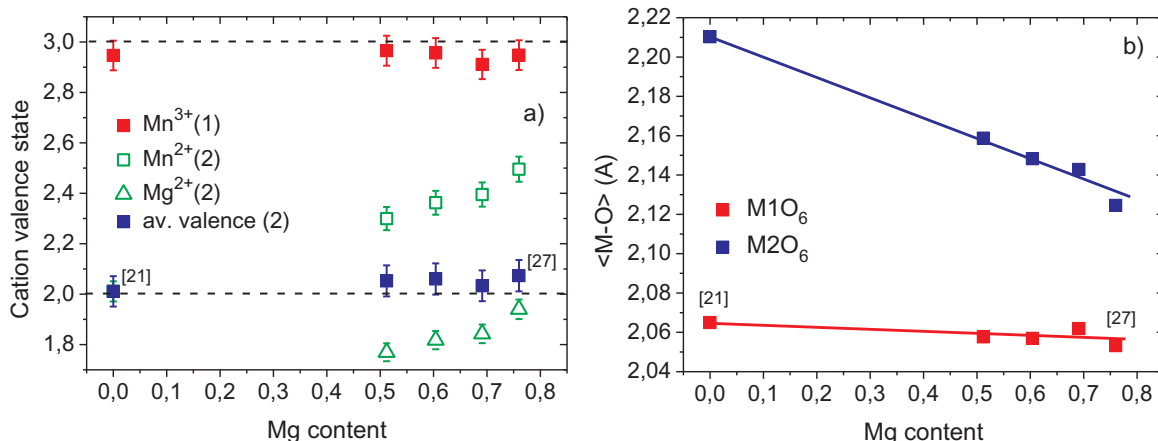


Fig. 5. a) Cation valence states at M1 and M2 sites as a function of the Mg content in $Mn_{2-x}Mg_xBO_4$. The dotted lines mark di- and trivalent cation states. b) Concentration dependences of the mean octahedral bond-lengths $\langle M-O \rangle$. The straight lines represent guides for the eye.

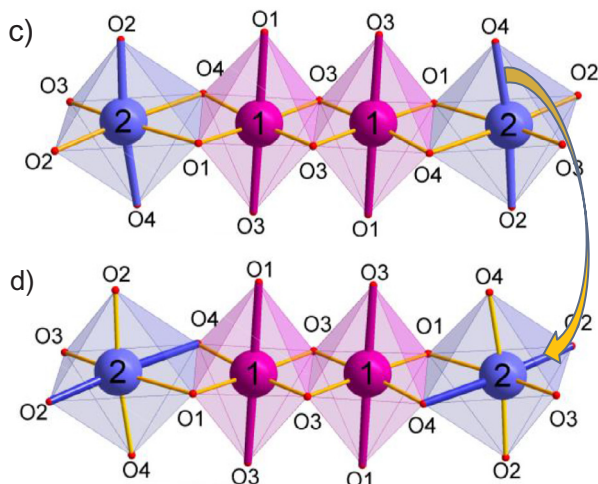
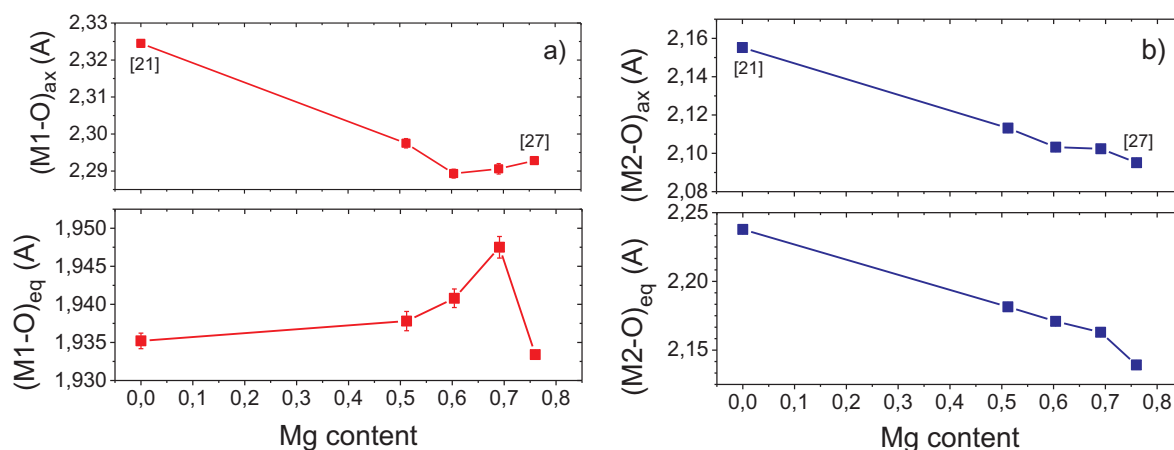


Fig. 6. Axial and equatorial bond lengths in M1O₆ (a) and M2O₆ (b) octahedra as a function of Mg content in $Mn_{2-x}Mg_xBO_4$ warwickites. c) and d) Arrow shows the change in the direction of the main octahedral axis corresponding to the compression of the M2O₆ octahedron for $x \leq 0.7$ (c) and $x \geq 0.76$ (d).

the cell parameters b and c decrease with increasing in Mg content, while the a parameter and angle β demonstrate non-monotonous behaviour. Such non-monotonous behaviour can be explained from the point of view of the change in the crystal structure distortions. Two main sources could be highlighted: 1) the difference in the size of the lattice sites, which is related with the difference in the ionic radii of the isomorphically substituting metals; 2) the peculiarities of the electronic structure of the ions (Jahn-Teller effect). The presented data show a

steady decrease of the parameters, including volume, under the reduction of the cation size ($r_1 = 0.83 \text{ \AA}$ for Mn^{2+} and 0.72 \AA for Mg^{2+}) to $x_c = 0.7$. Above this concentration, the change of the monoclinic distortions occurs, which manifests itself in the change of space group from $P2_1/n$ to $P2_1/a$.

To evaluate the oxidation states of Mn and Mg ions, a bond-valence-sum approach was applied [34]. The results are shown in Fig. 5(a). It can be clearly seen that the M1 site is occupied by the manganese ions

with the oxidation state 3+, while the M2 site is filled by the mixture of Mg²⁺ and Mn²⁺ ions. When the concentration increases, the effective charge of Mn ions at the M2 site shows an increment. It nevertheless has an exclusive size effect and is caused by the reduction in the interior distances < M2-O > due to the substitution of Mn²⁺ ions by the smaller Mg²⁺ ions (Fig. 5(b)). The average valence state of metal ions at the M2 site, accounting for the S.O.F., is found to be close to 2+. This result suggests that in the Mn_{2-x}Mg_xBO₄ solid solutions, the charge distribution over two non-equivalent metal sites has periodical character when the M1 position is occupied by only the trivalent ions and the M2 position is occupied by only the divalent ions. Such a situation does not occur in other heterometallic warwickites, which demonstrate a rather small difference in the charges of two metal sites (see below). The presence of charge ordering in Mn-Mg warwickites is probably caused by the strong electron-phonon coupling arising due to the local M1O₆ oxygen octahedral distortion.

As follows from crystal chemical principles, the transition metal ions prefer more distorted sites due to the energy gain of crystal field stabilisation. In the case of Mn³⁺ ions, the fivefold degenerated *d*-level splits into a threefold degenerated *t*_{2g}-level and a twofold degenerated *e*_g-level under the action of the crystalline field. This configuration of the degenerated orbitals is unstable and strong electron-phonon coupling arises. The electron-phonon coupling reduces the energy of the degenerated system by the lattice deformation and the lowering of its symmetry. This is accompanied by the local stretching along one of the octahedral axes and the simultaneous compression along the two others (Jahn-Teller theorem). In Mn₂BO₄, the M1O₆ octahedra have strong elongation along the O1-M1-O3 axes (axial bond), while the other four bonds (equatorial) are short. The Mg²⁺ substitution triggers the progressive compression of the axial bond and the simultaneous stretching of the equatorial bonds of M1O₆ octahedra (Fig. 6(a)). One can suggest that the observed deformation of M1O₆ leads to the reduction of *e*_g- and *t*_{2g}-levels splitting and, hence, to an increase in the stabilisation energy. In such a case, the energy gain can be obtained by the increase in the local octahedral distortions, typical for Mn³⁺ ions. This possibly occurred for the composition with *x* = 0.76 and manifested itself in the axial and equatorial bond changes.

As for M2O₆, for *x* = 0, this octahedron is compressed along the axial bond (O2-M2-O4) and has significant stretching in the equatorial plane. With the magnesium concentration increasing, the M2O₆ octahedron undergoes compression of all bond lengths (Fig. 6(b)). A rapid shortening of the equatorial bond lengths results in a change of the direction of the main octahedral axis. The direction of the main octahedral axis is changed, as shown in Fig. 6(c) and (d) for *x* ≤ 0.7 and *x* ≥ 0.76, respectively. The Mg substitution induces the changes in the local octahedral distortions of both metal sites, but mainly the M2 site, leading to the changes of the long-range monoclinic distortions reflecting in the P2₁/n → P2₁/a transformation.

3.2. Magnetisation

Field-cooled (FC) and zero-field-cooled (ZFC) *dc* magnetisation measurements were performed on a single crystal with an applied fields of 200 Oe and 10 kOe at different directions of the applied magnetic field relative crystallographic *c* axis. Fig. 7 shows the temperature dependence of the magnetic susceptibility of three compounds Mn_{2-x}Mg_xBO₄ at the applied field parallel to the *c* axis based on the FC magnetisation data. A sharp cusp in the temperature dependence of the magnetic susceptibility is shown. The critical temperatures are T_N = 16, 14 and 13 K for *x* = 0.5, 0.6 and 0.7, respectively. Down to the lowest temperatures, the FC and ZFC curves do not diverge (inset of Fig. 7). It is noteworthy that the irreversibility of the FC/ZFC magnetisation is characteristic behaviour in spin-glass systems and was observed in other heterometallic warwickites, such as MgFeBO₄, Mn_{2-x}Fe_xBO₄, Mg_{1-x}Co_xFeBO₄ [17,24].

The magnetic anisotropy was found to be small for all three Mn-Mg

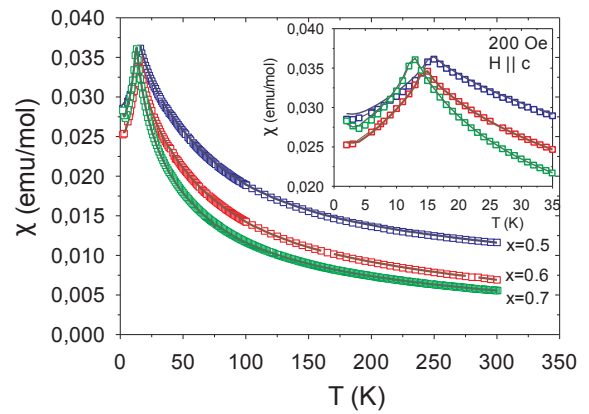


Fig. 7. Temperature dependences of magnetic susceptibility of Mn_{2-x}Mg_xBO₄ measured under a magnetic field of 200 Oe applied parallel to the *c* axis. The inset shows the ZFC (empty squares) and FC (solid lines) curves near the T_N.

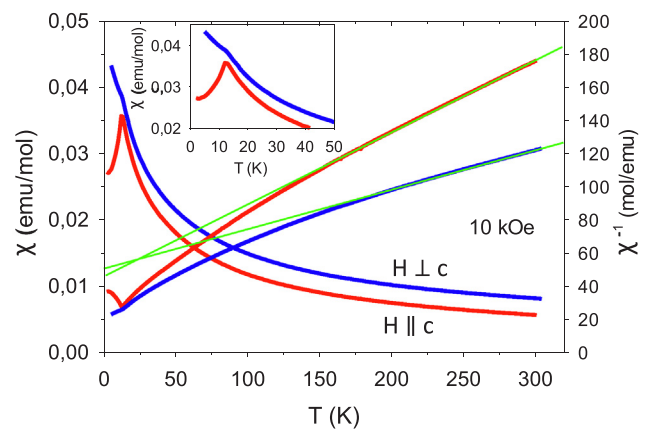


Fig. 8. FC magnetisations measured with an external magnetic field parallel and perpendicular to the *c* axis for Mn_{1.3}Mg_{0.7}BO₄. The inset shows the magnetic behaviour near the critical transition temperature.

warwickites, as can be observed from Fig. 8, where the magnetic data for *x* = 0.7 are drawn as an example. The *c* axis seems to be a hard magnetisation direction that is similar to Mn₂BO₄ [21] and CoFeBO₄ [17]. Below T_N, the FC magnetisation perpendicular to the *c* axis increases. The linear behaviour above 150 K indicates that the susceptibility obeys the Curie-Weiss law. A characteristic temperature at which the deviations appear is about one order of magnitude the T_N and close to that found in the spin-glass Mn_{2-x}Fe_xBO₄ [24] indicating the short-range spin correlations of the similar strength and sign in both Mn-Mg and Mn-Fe system. In Table 2, the Weiss temperature and an effective magnetic moment are listed for both orientations for all samples.

Assuming a high-spin state for all manganese ions, the magnetic moment per formula unit can be calculated as follows:

$$\mu_{\text{eff}} = \sqrt{(1-x) \cdot g^2 \cdot S_{\text{Mn}^{2+}} \cdot (S_{\text{Mn}^{2+}} + 1) + g^2 \cdot S_{\text{Mn}^{3+}} \cdot (S_{\text{Mn}^{3+}} + 1)},$$

where $S_{\text{Mn}^{2+}} = 5/2$, $S_{\text{Mn}^{3+}} = 2$, $g = 2$ for spin magnetism only (the last

Table 2
Magnetic parameters for Mn_{2-x}Mg_xBO₄ warwickite system.

	T _N (K)	θ (K)	μ _{eff} (μ _B /f.u.)	θ [⊥] (K)	μ _{eff} [⊥] (μ _B /f.u.)	μ _{eff} ^{av} (μ _B /f.u.)	μ _{eff} (μ _B /f.u.)
Mn ₂ BO ₄ [21]	26	-118	6.25	-134	6.95	6.72	7.68
Mn _{1.5} Mg _{0.5} BO ₄	16	-79	4.67	-146	6.05	5.63	6.30
Mn _{1.4} Mg _{0.6} BO ₄	14	-109	4.79	-202	6.19	5.76	6.08
Mn _{1.3} Mg _{0.7} BO ₄	13	-114	4.33	-213	5.79	5.35	5.96

column in Table 2).

Several interesting conclusions can be drawn from these measurements:

- (1) The effective magnetic moment decrease in the row of the samples $x = 0.5, 0.6$ and 0.7 , in agreement with the diamagnetic substitution $\text{Mn}^{2+} - \text{Mg}^{2+}$.
- (2) The values of μ_{eff}^{\perp} and $\mu_{\text{eff}}^{\parallel}$ indicate the magnetic anisotropy in the paramagnetic regime.
- (3) The average magnetic moment calculated as $\mu_{\text{eff}}^{\text{av}} = \sqrt{\frac{2 \cdot (\mu_{\text{eff}}^{\perp})^2 + (\mu_{\text{eff}}^{\parallel})^2}{3}}$ gives effective spin moments much lower than those expected for all samples.
- (4) The Weiss temperature is estimated to be negative for all samples. The diamagnetic substitution induces the enhancement of the nearest-neighbour antiferromagnetic interaction reflecting in the gradual increasing in Weiss temperature and points to a rather strong magnetic interaction between Mn^{3+} ions.
- (5) The substitution of the diamagnetic Mg^{2+} instead of magnetic Mn^{2+} led to a monotonic decrease in the Neel temperature.

A tentative interpretation of the low effective magnetic moment for $\text{Mn}_{2-x}\text{Mg}_x\text{BO}_4$ can be given as follows. Although the high-temperature interval of 150–300 K can be used to fit a straight line with high accuracy (the linearity coefficient $R = 0.999$), it is possible that the extension of the data to higher temperatures will yield an effective moment closer to the spin-only value. That is a complete paramagnetic state has not yet been reached, probably a somewhat degree of short-range order remains. Another possible explanation is there is a contribution of excited states to the average moment of the magnetic ions due to the unusual site symmetries in this structure.

The magnetisation curves below T_N exhibit straight lines characteristic of the AFM order. In Fig. 9, the magnetisation curves for all samples are presented.

3.3. Heat capacity

The heat capacity measured at $H = 0$ shows a quite pronounced anomalies near $T_N^{C(T)} = 14.2, 13.8$, and 12.1 K for $x = 0.5, 0.6$, and 0.7 , respectively (Fig. 10a). Note that $T_N^{C(T)}$ is slightly smaller than $T_N^{\chi(T)} = 16, 14$, and 13 and well coincides with the temperature for which $d\chi/dT$ becomes maxima (Fig. 10b). Hence, the observed λ -type anomalies can be attributed to a magnetic phase transitions.

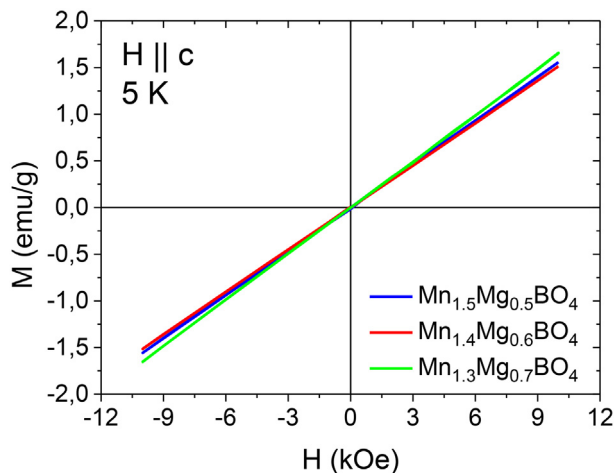


Fig. 9. Magnetisation curves of $\text{Mn}_{2-x}\text{Mg}_x\text{BO}_4$ warwickites measured at $T = 5$ K. The applied magnetic field is parallel to the c axis.

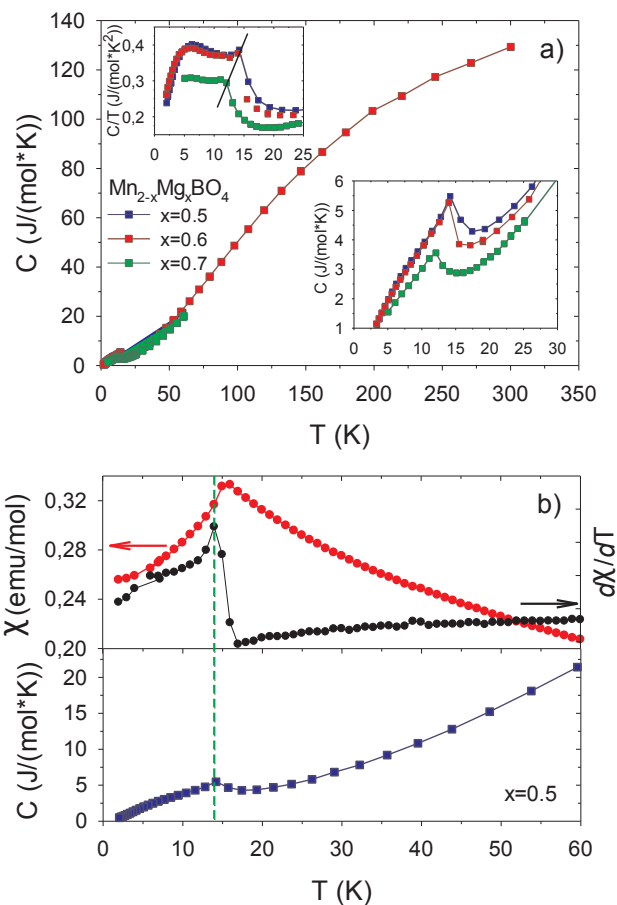


Fig. 10. a) Temperature dependences of the heat capacity measured at zero magnetic field for $\text{Mn}_{2-x}\text{Mg}_x\text{BO}_4$ warwickites. Top inset: specific heat plotted as C/T vs. T . The straight line shows the shift of T_N with Mg concentration. Bottom inset: the lambda point anomalies observed at the critical temperatures T_N . b) The top panel presents temperature dependences of the $\chi(T)$ and first derivative $d\chi/dT$. The bottom panel shows the heat capacity as a function of the temperature. The green vertical line indicates the coincidence of the critical temperatures obtained from the measurements of magnetic and thermodynamic properties. (For interpretation of the references to colour in this figure legend, the reader is referred to the web version of this article.)

3.4. High-field magnetisation of Mg-Mn heterometallic warwickites

To complement our studies on Mg-Mn warwickites, we have carried out isothermal magnetisation experiments at low temperatures, in order to better elucidate their ground-state properties. The measurements were performed for $\text{Mn}_{1.4}\text{Mg}_{0.6}\text{BO}_4$. Magnetic characterisation for one sample with a mass of 1.13 mg oriented perpendicular to H and three samples with a mass of 2.41 mg oriented parallel to H were carried out.

Fig. 11(a) and (b) show the field dependences of magnetisation at 4.2, 10, 12, 16 and 30 K for $H \parallel c$ and $H \perp c$, respectively. All curves demonstrate a rapid linear rise. However, for $H \parallel c$, this trend is followed by an abrupt increase of the magnetisation above $H_{C1} = 35$ kOe (at 4.2 K). Above $H_{C2} = 64$ kOe, the magnetisation again shows linear behaviour with a larger value of slope. This can be more clearly seen from the dM/dH plot (inset to Fig. 11(a)). The appearance of the peaks in dM/dH is an indication of a spin-flop transition. With increasing temperatures, this feature is weakened and disappears at 16 K. The peak position of dM/dH decreases from $H_{SF} = 61$ kOe at 4.2 K to 33 kOe at 12 K. Field-sweep experiments at 4.2 K showed that the spin-flop appears at slightly different magnetic fields when the magnetic field increases and decreases, suggesting the existence of a small magnetic anisotropy. For $H \perp c$, the magnetisation shows typical

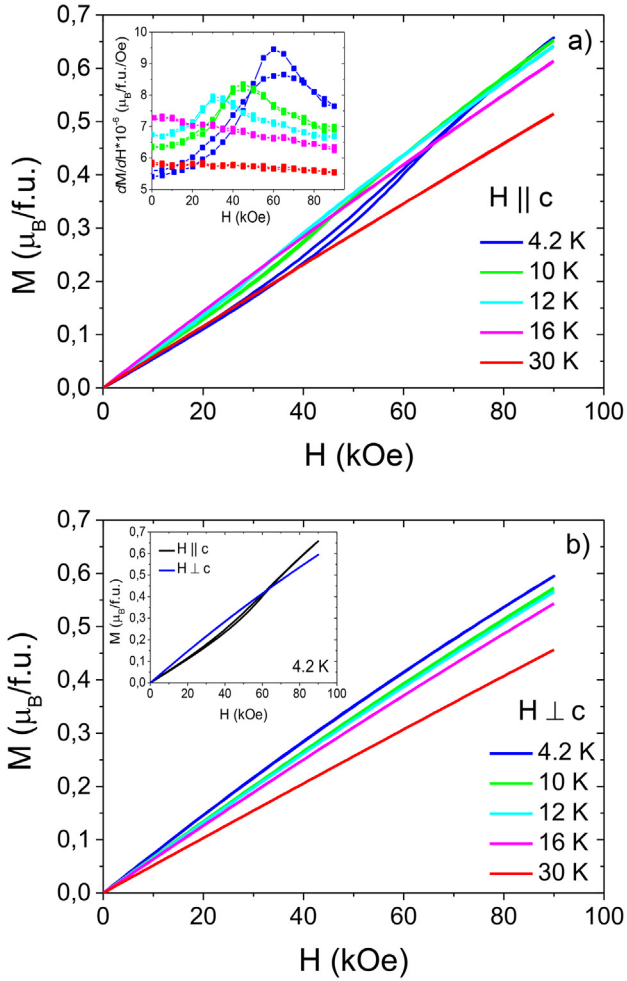


Fig. 11. Magnetisation isotherms for $\text{Mn}_{1.4}\text{Mg}_{0.6}\text{BO}_4$ measured with magnetic fields applied parallel (a) and perpendicular (b) to the c axis. The inset to (a) is the derivatives dM/dH at various temperatures, revealing the decreasing of the spin-flop field with temperature. The inset to (b) shows the changing of the magnetic anisotropy from easy-plane to easy axis at $H_{C2} = 64$ kOe.

antiferromagnetic behaviour and ML increases linearly with H up to H_{C1} , showing the deviation from linearity above this field.

The magnitudes of the initial susceptibilities ($H < H_{SF}$) are $\chi_{\perp} = 7.34 \cdot 10^{-6} \mu_B/\text{f.u.}/\text{Oe}$ and $\chi_{\parallel} = 5.45 \cdot 10^{-6} \mu_B/\text{f.u.}/\text{Oe}$ for the perpendicular and parallel directions of the external field, respectively. The small anisotropy of the magnetic response suggests that the ordered magnetic moments of Mn ions have both in-plane and out-of-plane components. The extrapolation to zero field of the M_{\parallel} data in high fields has a negative intercept to the magnetisation axis, suggesting the net moment is generated during the phase transition. The spin-flop transition can be further analysed by subtracting the linear contribution (antiferromagnetic component) shown as a dashed line in Fig. 12. Above H_{C1} , the magnetic moment ΔM undergoes the reorientation process, to be parallel to the applied field, which allows an additional contribution to the total magnetisation along the c axis. The magnitude of the increased magnetic moment $\Delta M = 0.017 \mu_B/\text{f.u.}$ at 4.2 K and gradually decreases as the temperature increases (inset to Fig. 12). Note that the end member Mn_2BO_4 shows the spin-flop transition at $H_{SF} = 24$ kOe when the external field is applied perpendicular to the c axis. Different from MgMn, the extrapolation of magnetisation of MnMn in the high fields goes straight across the origin, suggesting no net moment appears at the transition. The fact that the magnetic susceptibility of the MgMn sample is very close to that found for MnMn (χ_{\perp} (4.2 K) = $4.02 \cdot 10^{-6} \mu_B/\text{f.u.}/\text{Oe}$), reflecting that at low temperatures,

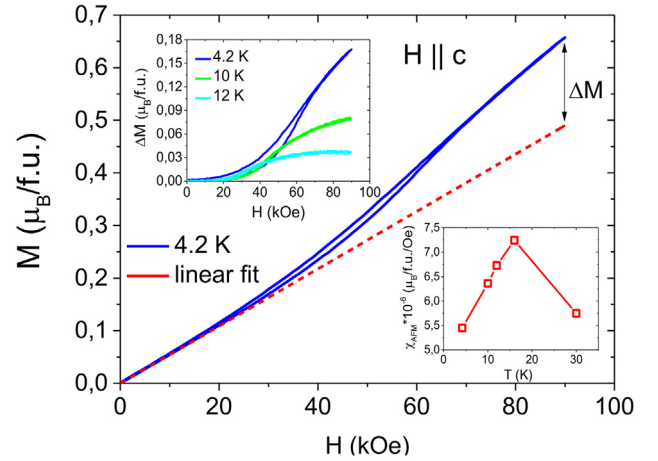


Fig. 12. Magnetisation isotherm at 4.2 K for single crystal $\text{Mn}_{1.4}\text{Mg}_{0.6}\text{BO}_4$ measured with an applied magnetic field along the c axis. The top inset shows a magnetic moment ΔM obtained by subtracting linear dependence (dashed line) from the raw data. The bottom inset is a temperature dependence of the antiferromagnetic susceptibility, determined at the low-field range ($H < H_c$). The maximum of $\chi_{AFM}(T)$ curve occurs near to $T_N = 14$ K.

the antiferromagnetic interactions prevail, leading to antiparallel alignment of the manganese magnetic moment and hence, to antiferromagnetic ordering.

The observed spin-flop transition in MgMn can be rationalised by adopting the concept of several interpenetrating sublattices, usually employed to describe antiferromagnets where each sublattice consists of the chains of magnetic ions. The diamagnetic substitution of Mn^{2+} ions by Mg^{2+} ions leads to the weakening of the exchange interactions both $\text{Mn}^{2+}-\text{Mn}^{2+}$ and $\text{Mn}^{3+}-\text{Mn}^{2+}$. A sufficient external field H_{C2} overwhelms the weak AF interactions and causes the reorientation process of the weakly-coupled magnetic component. As a result, there occurs the change of the magnetic anisotropy from easy-plane (ab plane) for $H < H_{C2}$ to easy-axis (c axis) for $H > H_{C2}$.

The obtained magnetic data of the $\text{Mn}_{1.4}\text{Mg}_{0.6}\text{BO}_4$ sample can be summarised as follows. The magnetic interaction between manganese ions is antiferromagnetic, resulting in the antiparallel alignment. The AFM, SF and PM states were observed under certain conditions. The phase transition from PM to the long-range AFM state with $T_N = 14$ K regardless of the external magnetic field. At $T < T_N$, the low field and temperature stabilise the AFM phase, while the high field and temperature causes the SF phase. The complete magnetic characterisation allows building the magnetic phase diagram (Fig. 13).

4. Discussion

It is interesting to compare two substituted systems $\text{Mn}_{2-x}\text{Mg}_x\text{BO}_4$ and $\text{Mn}_{2-x}\text{Fe}_x\text{BO}_4$, which undergo magnetic transitions with close values of the critical temperatures, but, however, quite different in nature (Fig. 14). In Mn_2BO_4 the lowering of the symmetry from the orthorhombic (Pnma) warwickite structure to the monoclinic ($P2_1/n_1$) occurs through the cooperative Jahn-Teller distortions to minimise the elastic energy. The same distortions, but decreasing in strength, are present in the solid solutions of $\text{Mn}_{2-x}\text{Mg}_x\text{BO}_4$ showing a monoclinic structure, isomorphous to the structure of Mn_2BO_4 . This behaviour reflects strong electro-phonon coupling of Mn^{3+} ions, which are prone to occupying the M1 site in the $\text{Mn}_{2-x}\text{Mg}_x\text{BO}_4$ system. In $\text{Mn}_{2-x}\text{Fe}_x\text{BO}_4$ warwickites, the Fe^{3+} is not a J-T ion and prefers a fairly symmetric coordination environment. This conformation disrupts the simultaneous formation of both long and short bonds at a given site, thereby reducing the stabilisation of the local distortions. The octahedrally symmetric Fe^{3+} and the J-T active Mn^{3+} ions are disordered over crystallographic sites, rather, it is more likely that J-T distortions are present locally but the

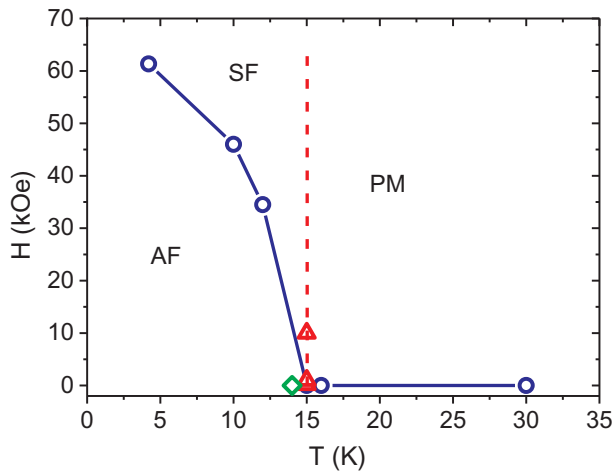


Fig. 13. Magnetic phase diagrams for $Mn_{1.4}Mg_{0.6}BO_4$ warwickite. The blue circles are data obtained from the $M(H)$ curves, the red triangles are from the $\chi_{dc}(T)$ curves and the green diamond is from $C_p(T)$ curve. The solid and dotted lines are a guide to the eye. (For interpretation of the references to colour in this figure legend, the reader is referred to the web version of this article.)

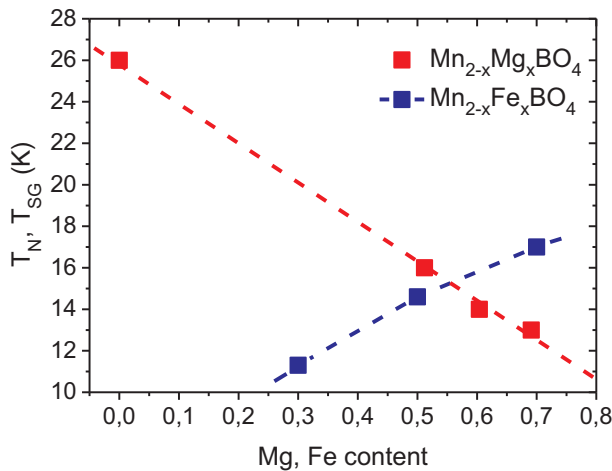


Fig. 14. Magnetic critical temperature as a function of the concentration for the warwickite systems $Mn_{2-x}Mg_xBO_4$ and $Mn_{2-x}Fe_xBO_4$. The dashed lines are guides for the eye.

orientation of these distortions is disordered. This leads to the inability to develop the long-range ordered pattern of occupied orbitals. The disappearance of the orbital order causes the break of the charge ordering. The random cation distribution is the reason for magnetic disorder in $Mn_{2-x}Fe_xBO_4$ [17,24].

Finally, we discuss the prerequisites for the occurrence of cation ordering in heterometallic warwickites. In this sense, magnesium-based warwickites $MgMBO_4$, where M is a trivalent metal ion, are promising systems in which to search for cation order, since Mg^{2+} allows us to study the size and the octahedral distortion effects of the M ion when the latter is varied. The known experimental studies give not numerous structural data on the $MgMBO_4$ warwickite, where $M = Ti^{3+}$ [35], V^{3+} [12], Fe^{3+} [36], Sc^{3+} [27], Ga^{3+} [37], In^{3+} [38], Ta^{5+} [39] and Nb^{5+} [39]. Only these compounds were chosen for which crystal structure analyses were available. In order to quantify the match of Mg^{2+} and M^{3+} ions to the cation order, we used two main parameters: the charge difference between two metal sites M1 and M2 (ΔCD) and the octahedral distortion parameter (Δ). The former depends on the cation distribution over non-equivalent sites and directly reflects the cation order. There exist two end cases corresponding to a completely random distribution (ΔCD equals zero) and completely ordered distribution

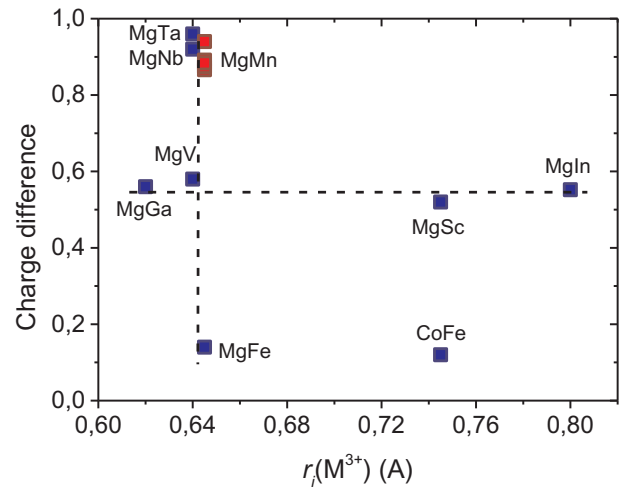


Fig. 15. Charge difference between two metal sites (v.u.) in the magnesium-containing warwickites. The available data for $CoFeBO_4$ are presented also.

(ΔCD equals unity). A quantitative measure of the magnitude of the local distortion is given by the octahedral distortion parameter $\Delta = \frac{1}{6} \sum_{i=1,6} \left[\frac{d_i - d}{d} \right]^2$, where d_i is an individual M–O bond-length and d is a mean $\langle M-O \rangle$.

The data are shown in Figs. 15 and 16. Continuing from $MgGaBO_4$ to $MgInBO_4$, the difference in the ionic radii of metal ions actually increases ($r_{Ga^{3+}} = 0.620$, $r_{V^{3+}} = 0.640$, $r_{Sc^{3+}} = 0.745$ and $r_{In^{3+}} = 0.800$ Å), yet the character of the cation distribution is preserved. In contrast, for the Fe^{3+} , V^{3+} , Ta^{5+} , Nb^{5+} and Mn^{3+} ions with close ionic radii, the situation is varied from almost cation disordered $\Delta CD \sim 0.1$ v.u. (for $MgFe$) to a high degree of cation order $\Delta CD \sim 0.9$ v.u. (for $MgMn$, $MgTa$ and $MgNb$). All considered warwickites exhibit the distortion of the $M1O_6$ octahedron, a much larger distortion than that $M2O_6$. It is obvious the hetero-metallic warwickites $MgMn$, $MgTa$, $MgNb$ exhibiting the cation order show a highest distortion parameter Δ . While the cation-disordered compounds tend to have a lower

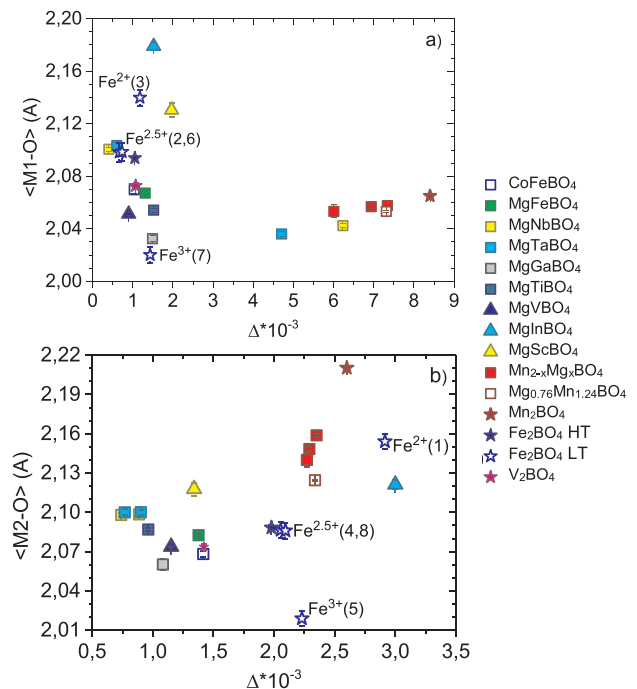


Fig. 16. Mean M–O bond lengths as a function of the distortion for $M1O_6$ (a) and $M2O_6$ (b) octahedra. The error-bars are taken from the original works.

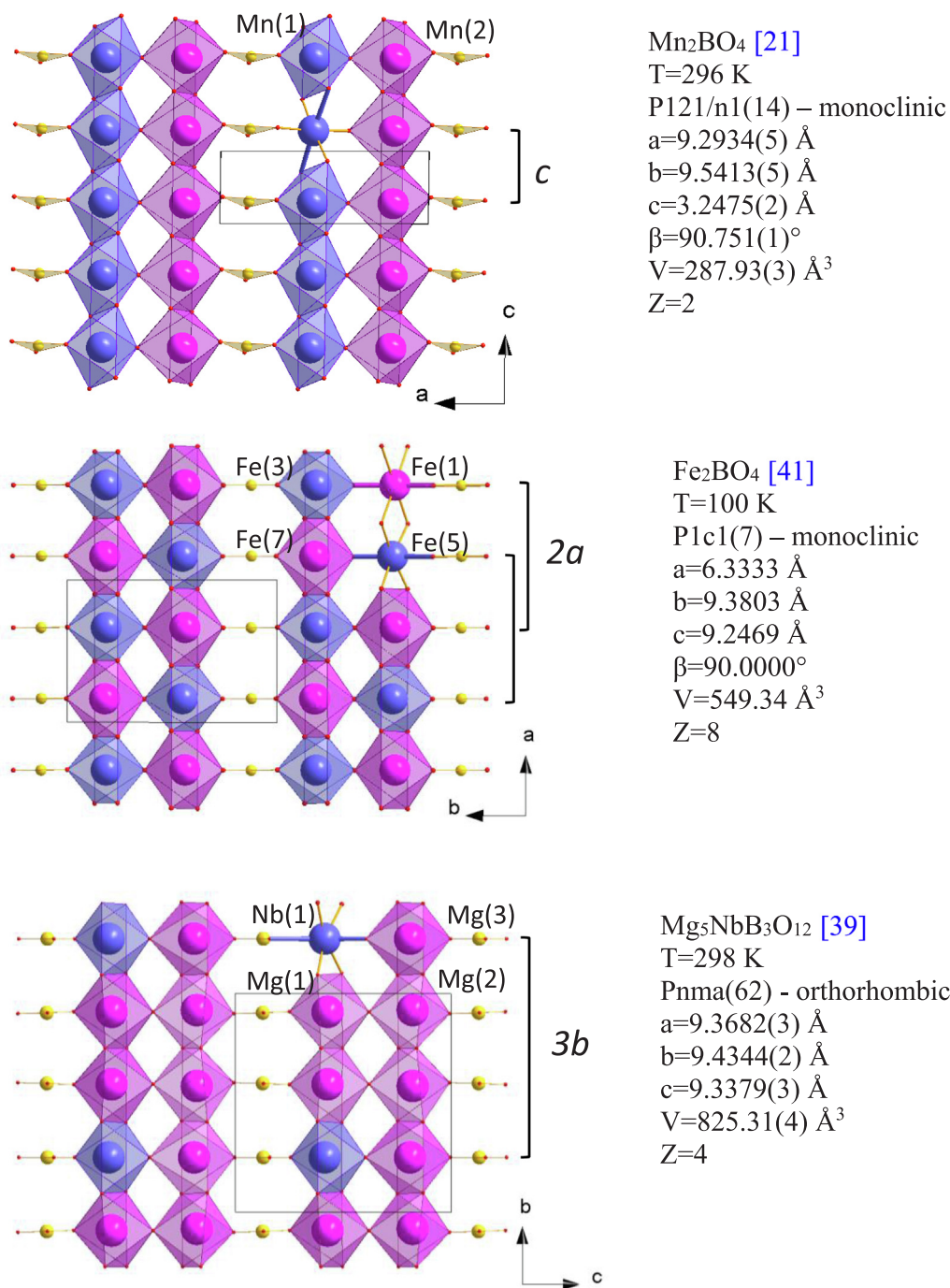


Fig. 17. The ordering of the local octahedral distortions in cation- and charge-ordered warwickites resulting in the doubling and tripling of the short crystallographic axis, as found in Mn₂BO₄ (a), Fe₂BO₄ (b), and Mg₅NbB₃O₁₂ (c). The double chains of metal ions separated by the (BO₃) groups form the planes shown in Fig. 1. The main axes of the octahedra, showing the largest distortion parameter are highlighted in bold.

distortion parameter for both metal sites. Therefore, there is interrelation between the cation order and local octahedral distortion. The latter can also be enhanced by chemical pressure induced by oversized M³⁺ ions, as demonstrated by the behaviour of MgInBO₄ ($\Delta(M2) = 3.0 \cdot 10^{-3}$).

Unlike the Mg-Mn warwickite, the compounds Mg₅TaB₃O₁₂ and Mg₅NbB₃O₁₂ have a strong driving force for the cation ordering as a result of the oxidation state difference of three between the Mg²⁺ and Ta⁵⁺/Nb⁵⁺ ions. Additionally, these compounds exhibit a large octahedral distortions of $\Delta(M1) = 4.71 \cdot 10^{-3}$ and $6.23 \cdot 10^{-3}$ for Ta and Nb, respectively. Following the above assumption that the magnetic order is

a consequence of the cation order and, hence a charge order, one can expect an existence of long-range order in the heterometallic warwickites containing the pentavalent ions. We can therefore report that our preliminary results on the study of a novel cation-ordered warwickite Co₅NbB₃O₁₂ have confirmed this assumption [40].

The fact that the octahedral site cation ordering is influenced by the ordering of the local distortions is confirmed by the similar analysis performed for the homometallic compounds (they are also shown in Fig. 16). For V₂BO₄, only the room-temperature crystal structure data are available in the literature [23]. The high resolution synchrotron powder X-ray diffraction experiment revealed the orthorhombic

symmetry (*Pnma*, No.62). The sites V1 and V2 have similar $<M-O>$ bond lengths and close values of distortion parameters. Nevertheless, the authors reported changes in the crystallographic symmetry upon cooling between 295 and 90 K, which is interpreted as the occurrence of the charge ordering. Fe_2BO_4 exhibits a much larger local distortions ($\Delta Fe1$ and $\Delta Fe5$) for the monoclinic phase (*P1c1*, No.7) ($T = 100\text{ K} < T_{CO}$) than that for the orthorhombic one (*Pmnb*, No.62) ($T = 355\text{ K} > T_{CO}$) [41]. The transition to the charge ordering state is accompanied by the doubling of the short crystallographic parameter. With the higher symmetry, the even bond length distribution can be realised with tripling of the short axis, as found in $Mg_5NbB_3O_{12}$ and $Mg_5TaB_3O_{12}$ [39] (Fig. 17).

From the above analysis, it is possible to draw the conclusion that the difference in the ionic radii is an insufficient factor for stabilising the cation order in the warwickites, but this lead to the idea that the local octahedral distortions is a key to the understanding of magnetic and electronic phenomena in these materials.

5. Conclusion

In summary, we have investigated the structural, magnetic and thermodynamic properties of the heterometallic warwickites $Mn_{2-x}Mg_xBO_4$ with $x = 0.5, 0.6$ and 0.7 . All samples were found to crystallise in a monoclinic $P2_1/n$ symmetry similar to the end member Mn_2BO_4 .

The lattice parameters display a monotonic change with the magnesium concentration. The local octahedral distortions associated with the Jahn-Teller effect of Mn^{3+} ions are persistent for all solid solutions, albeit reduced compared with that of Mn_2BO_4 . A regular occupation of the M2 site by the Mg^{2+} ions was found in contrast with other heterometallic warwickites where cation disorder has a large effect. As a result, the charge distribution over two metal sites has a character of $Mn^{3+}(1)$ and $Mn^{2+}(2)/Mg^{2+}(2)$.

To the best of our knowledge, the $Mn_{2-x}Mg_xBO_4$ system is the first example of a heterometallic warwickite showing long-range order. Magnetic and thermodynamic measurements show that all samples undergo a transition from paramagnetic to an antiferromagnetic ordering state at the Neel temperatures $T_N = 16, 14$ and 13 K . The magnetic anisotropy is small with the c axis as a hard magnetisation direction at low fields. Careful investigation in the ordered state allows for the building of a magnetic phase diagram.

The next important finding is that the long-range magnetic order in heterometallic warwickites can appear as a consequence of the cation and charge order. The latter, in turn, arises from the ordering of the J-T distortions. The ability of the system to develop the long-range pattern of the octahedral distortions results in the appearance of the charge ordering. This analysis is useful in understanding the basic electronic and magnetic properties of the warwickites.

CRedit authorship contribution statement

N.V. Kazak: Conceptualization, Methodology, Funding acquisition. **N.A. Belskaya:** Data curation, Investigation. **E.M. Moshkina:** Investigation, Visualization, Funding acquisition. **L.N. Bezmaternykh:** Investigation. **A.D. Vasiliev:** Investigation. **S.N. Sofronova:** Investigation. **R.M. Eremina:** Data curation, Investigation. **E.V. Eremin:** Investigation. **A.R. Muftakhutdinov:** Data curation, Investigation. **M.A. Cherosov:** Data curation, Investigation. **S.G. Ovchinnikov:** Supervision.

Declaration of Competing Interest

The authors declare that they have no known competing financial interests or personal relationships that could have appeared to influence the work reported in this paper.

Acknowledgements

The reported study was funded by the Russian Foundation for Basic Research (no. 20-02-00559), Government of Krasnoyarsk Territory, Krasnoyarsk Regional Fund of Science to the research project № 18-42-243007.

Appendix A. Supplementary data

Supplementary data to this article can be found online at <https://doi.org/10.1016/j.jmmm.2020.166820>.

References

- [1] A. Bloise, E. Barrese, Synthesis of isomorphic vonsenite-ludwigite series, *Neues Jahrbuch für Mineralogie-Abhandlungen: J. Mineral. Geochem.* 186 (2009) 345–350, <https://doi.org/10.1127/0077-7757/2009/0153>.
- [2] P.W.U. Appel, S. Bigi, M.F. Brigatti, Crystal structure and chemistry of yuanfuliite and its relationships with warwickite, *Eur. J. Mineral.* (1999) 483–492, <https://doi.org/10.1127/ejm/11/3/0483>.
- [3] J.P. Attfield, J.F. Clarke, D.A. Perkins, Magnetic and crystal structures of iron borates, *Phys. B* 180 (1992) 581–584, [https://doi.org/10.1016/0921-4526\(92\)90401-D](https://doi.org/10.1016/0921-4526(92)90401-D).
- [4] P. Bordet, E. Suard, Magnetic structure and charge ordering in Fe_3BO_5 : a single-crystal x-ray and neutron powder diffraction study, *Phys. Rev. B* 79 (2009) 144408, <https://doi.org/10.1103/PhysRevB.79.144408>.
- [5] J. Bartolomé, A. Arauzo, N.V. Kazak, N.B. Ivanova, S.G. Ovchinnikov, Yu V. Knyazev, I.S. Lyubutin, Uniaxial magnetic anisotropy in $Co_2.25Fe_0.75O_2BO_3$ compared to $Co_3O_2BO_3$ and $Fe_3O_2BO_3$ ludwigites, *Phys. Rev. B* 83 (2011) 144426. [Doi:10.1103/PhysRevB.83.144426](https://doi.org/10.1103/PhysRevB.83.144426).
- [6] D.C. Freitas, C.P.C. Medrano, D.R. Sanchez, M.N. Regueiro, J.A. Rodríguez-Velamazán, M.A. Continentino, Magnetism and charge order in the ladder compound $Co_3O_2BO_3$, *Phys. Rev. B* 94 (2016) 174409, <https://doi.org/10.1103/PhysRevB.94.174409>.
- [7] J. Larrea, D.R. Sanchez, F.J. Litterst, E.M. Baggio-Saitovitch, Charge delocalization in the ludwigite $Fe_3O_2BO_3$, *J. Phys.: Condens. Matter* 13 (2001) L949, <https://doi.org/10.1088/0953-8984/13/48/105>.
- [8] T.G. Rappoport, L. Ghivelder, J.C. Fernandes, R.B. Guimaraes, M.A. Continentino, Experimental observation of quantum entanglement in low-dimensional spin systems, *Phys. Rev. B* 75 (2007) 054422, <https://doi.org/10.1103/PhysRevB.75.054422>.
- [9] R.B. Guimaraes, J.C. Fernandes, M.A. Continentino, H.A. Borges, C.S. Moura, J.B.M. Da Cunha, C.A. Dos Santos, Dimensional crossover in magnetic warwickites, *Phys. Rev. B* 56 (1997) 292, <https://doi.org/10.1103/PhysRevB.56.292>.
- [10] G.R. Hearne, W.N. Sibanda, E. Carleschi, V. Pischedda, J.P. Attfield, Pressure-induced suppression of charge order and nanosecond valence dynamics in Fe_2OBO_3 , *Phys. Rev. B* 86 (2012) 195134, <https://doi.org/10.1103/PhysRevB.86.195134>.
- [11] Maolin Dong, Quan Kuang, Xinxuan Zeng, Lei Chen, Jianzhong Zhu, Qinghua Fan, Youzhong Dong, Yanming Zhao, Mixed-metal borate $FeVO_4$ of tunnel structure: synthesis and electrochemical properties in lithium and sodium ion batteries, *J. Alloy. Compd.* 812 (2020) 152165, <https://doi.org/10.1016/j.jallcom.2019.152165>.
- [12] S.-H. Bo, C.P. Grey, P.G. Khalifah, Defect-tolerant diffusion channels for Mg^{2+} ions in ribbon-type borates: structural insights into potential battery cathodes $MgVBO_4$ and $Mg_xFe_{2-x}B_2O_5$, *Chem. Mater.* 27 (2015) 4630–4639, <https://doi.org/10.1021/acs.chemmater.5b01040>.
- [13] V. Pralong, B. Le Roux, S. Malo, A. Guesdon, F. Lainé, J.F. Colin, C. Martin, Electrochemical activity in oxyborates toward lithium, *J. Solid State Chem.* 255 (2017) 167–171, <https://doi.org/10.1016/j.jssc.2017.08.010>.
- [14] H. Neuendorf, W. Günßer, Transition from quasi-one-dimensional to spin-glass behaviour in insulating $FeMg_2BO_5$, *J. Magn. Magn. Mater.* 173 (1997) 117–125, [https://doi.org/10.1016/S0304-8853\(97\)00171-6](https://doi.org/10.1016/S0304-8853(97)00171-6).
- [15] R. Ma, D. Xu, Y. Yang, X. Su, B. Lei, Z. Yang, S. Pan, $ScMO(BO_3)$ ($M = Ca$ and Cd): new Sc-based oxyborates featuring interesting edge-sharing sandwich-like chains and UV cut-off edges, *Dalton Trans.* 46 (2017) 14839–14846, <https://doi.org/10.1039/C7DT03172F>.
- [16] J. Kumar, S.N. Panja, D.J. Mukkattukavil, A. Bhattacharyya, A.K. Nigam, S. Nair, Reentrant superspin glass state and magnetization steps in the oxyborate Co_2AlBO_5 , *Phys. Rev. B* 95 (2017) 144409, <https://doi.org/10.1103/PhysRevB.95.144409>.
- [17] A. Arauzo, N.V. Kazak, N.B. Ivanova, M.S. Platonov, Y.V. Knyazev, O.A. Bayukov, L.N. Bezmaternykh, I.S. Lyubutin, K.V. Frolov, S.G. Ovchinnikov, J. Bartolomé, Spin-glass behavior in single crystals of hetero-metallic magnetic warwickites $MgFeBO_4$, $Mg_{0.5}Co_{0.5}FeBO_4$, and $CoFeBO_4$, *J. Magn. Magn. Mater.* 392 (2015) 114–125, <https://doi.org/10.1016/j.jmmm.2015.05.006>.
- [18] I.S. Lyubutin, N. Yu. Korotkov, K.V. Frolov, N.V. Kazak, M.S. Platonov, Yu. V. Knyazev, L.N. Bezmaternykh, S.G. Ovchinnikov, A. Arauzo, J. Bartolomé, Spin-glass behavior of warwickite $MgFeBO_4$ and $CoFeBO_4$ crystals observed by Mössbauer spectroscopy, *J. Alloy. Compd.* 642 (2015) 204–209, <https://doi.org/10.1016/j.jallcom.2015.04.067>.
- [19] J.C. Fernandes, R.B. Guimaraes, M.A. Continentino, H.A. Borges, J.V. Valarelli, A. Lacerda, Titanium-III warwickites: a family of one-dimensional disordered

- magnetic systems, Phys. Rev. B 50 (1994) 16754, <https://doi.org/10.1103/PhysRevB.50.16754>.
- [20] R.J. Goff, A.J. Williams, J.P. Attfield, Spin, charge, and orbital order in Mn_2OBO_3 , Phys. Rev. B 70 (2004) 014426, <https://doi.org/10.1103/PhysRevB.70.014426>.
- [21] N.V. Kazak, M.S. Platonov, Yu.V. Knyazev, N.B. Ivanova, O.A. Bayukov, A.D. Vasiliev, L.N. Bezmaternykh, V.I. Nizhankovskii, S.Yu. Gavrilkin, K.V. Lamonova, S.G. Ovchinnikov, Uniaxial anisotropy and low-temperature antiferromagnetism of Mn_2BO_4 single crystal, J. Magn. Magn. Mater. 393 (2015) 316–324, <https://doi.org/10.1016/j.jmmm.2015.05.081>.
- [22] J.P. Attfield, A.M.T. Bell, L.M. Rodriguez-Martinez, J.M. Greneche, R.J. Cernik, J.F. Clarke, D.A. Perkins, Electrostatically driven charge-ordering in Fe_2OBO_3 , Nature 396 (1998) 655, <https://doi.org/10.1038/25309>.
- [23] E.M. Carnicom, K. Górnicka, T. Klimczuk, R.J. Cava, The homometallic warwickite V_2OBO_3 , J. Solid State Chem. 265 (2018) 319–325, <https://doi.org/10.1016/j.jssc.2018.06.021>.
- [24] N.V. Kazak, M.S. Platonov, Yu.V. Knyazev, E.M. Moshkina, S.Yu. Gavrilkin, O.A. Bayukov, M.V. Gorev, E.I. Pogoreltsev, G.M. Zeer, S.M. Zharkov, S.G. Ovchinnikov, Fe-induced enhancement of antiferromagnetic spin correlations in $\text{Mn}_{2-x}\text{Fe}_x\text{BO}_4$, J. Magn. Magn. Mater. 452 (2018) 90–99, <https://doi.org/10.1016/j.jmmm.2017.12.037>.
- [25] M.S. Platonov, N.V. Kazak, Yu.V. Knyazev, L.N. Bezmaternykh, E.M. Moshkina, A.L. Trigub, A.A. Veligzhanin, Y.V. Zubavichus, L.A. Solovyov, D.A. Velikanov, S.G. Ovchinnikov, Effect of Fe-substitution on the structure and magnetism of single crystals $\text{Mn}_{2-x}\text{Fe}_x\text{BO}_4$, J. Cryst. Growth 475 (2017) 239–246, <https://doi.org/10.1016/j.jcrysgro.2017.06.026>.
- [26] R.D. Shannon, Acta Crystallogr. A 32 (1976) 751, <https://doi.org/10.1107/S0567739476001551>.
- [27] R. Norrestam, Structural investigation of two synthetic warwickites: undistorted orthorhombic MgScOBO_3 and distorted monoclinic $\text{Mg}_{0.76}\text{Mn}_{1.24}\text{OBO}_3$, Zeitschrift für Kristallographie-Crystallogr. Mater. 189 (1989) 1–12. Doi:10.1524/zkri.1989.189.14.1.
- [28] R.M. Eremina, E.M. Moshkina, A.R. Muftakhutdinov, I.F. Gilmutdinov, N.M. Lyadov, Magnetic properties of the warwickite MnMgBO_4 , Solid State Commun. 290 (2019) 64–66, <https://doi.org/10.1016/j.ssc.2018.12.019>.
- [29] G.M. Sheldrick, A short history of SHELX, Acta Cryst. A 64 (2008) 112–122, <https://doi.org/10.1107/S0108767307043930>.
- [30] G.M. Sheldrick, SHELXS and SHELXL97, in: Program for Crystal Structure Refinement, University of Göttingen, Germany, 1997.
- [31] Supplementary Materials for XRD data for: Antiferromagnetism of the cation-ordered warwickite system $\text{Mn}_{2-x}\text{Mg}_x\text{BO}_4$ ($x = 0.5, 0.6$ or 0.7). Details of the refined structures are deposited in the Inorganic Crystal Structure Database with accession numbers 1980579, 1980582, 1980588.
- [32] A. Utzolino, K. Bluhm, New insights into the stabilization of the hulsite structure during crystal structure determination of $\text{MnII}_2\text{MnIII}(\text{BO}_3)_2$ and $\text{MnIISrMnIII}(\text{BO}_3)_2$, Zeitschrift für Naturforschung B 51 (10) (1996) 1433–1438, <https://doi.org/10.1515/znB-1996-1012>.
- [33] J.J. Cooper, R.J.D. Tilley, New oxyborates in the Mg-Mn-B-O system, J. Solid State Chem. 63 (2) (1986) 129–138, [https://doi.org/10.1016/0022-4596\(86\)90162-3](https://doi.org/10.1016/0022-4596(86)90162-3).
- [34] I.D. Brown, D. Altermatt, Acta Cryst. B 41 (1985) 244–247, <https://doi.org/10.1107/S0108768185002063>.
- [35] Tetsuya Kawano, Hisanori Yamane, Redetermination of synthetic warwickite, $\text{Mg}_3\text{TiO}_2(\text{BO}_3)_2$, Acta Crystallographica Section E 67 (2011) i18–i19, <https://doi.org/10.1107/S1600536811002157>.
- [36] N.V. Kazak, M.S. Platonov, Yu.V. Knyazev, N.B. Ivanova, Y.V. Zubavichus, A.A. Veligzhanin, A.D. Vasiliev, L.N. Bezmaternykh, O.A. Bayukov, A. Arauzo, J. Bartolome, K.V. Lamonova, S.G. Ovchinnikov, Crystal and local atomic structure of MgFeBO_4 , $\text{Mg}_{0.5}\text{Co}_{0.5}\text{FeBO}_4$, and CoFeBO_4 : Effects of Co substitution, Phys. Status Solidi B 252 (2015) 2245–2258, <https://doi.org/10.1002/pssb.201552143>.
- [37] Z. Yang, X.L. Chen, J.K. Liang, Y.C. Lan, T. Xu, Phase relations in the $\text{MgO-Ga}_2\text{O}_3\text{-B}_2\text{O}_3$ system and the crystal structure of MgGaBO_4 , J. Alloy. Compd. 319 (2001) 247–252, [https://doi.org/10.1016/S0925-8388\(01\)00871-4](https://doi.org/10.1016/S0925-8388(01)00871-4).
- [38] H.K. Li, G.M. Cai, J.J. Fan, Z.P. Jin, T.T. Zhou, X.L. Chen, Crystal structures of two novel borate compounds MgInBO_4 and $\text{MgIn}_7/8\text{B}_7/8\text{O}_{29/8}$, J. Solid State Chem. 202 (2013) 262–268, <https://doi.org/10.1016/j.jssc.2013.03.060>.
- [39] T. Kawano, H. Yamane, Synthesis, crystal structures and photoluminescence properties of new oxyborates, $\text{Mg}_5\text{NbO}_3(\text{BO}_3)_3$ and $\text{Mg}_5\text{TaO}_3(\text{BO}_3)_3$, with novel warwickite-type superstructures, J. Solid State Chem. 184 (2011) 2466–2471, <https://doi.org/10.1016/j.jssc.2011.07.022>.
- [40] Needle-shaped single crystals of $\text{Co}_5\text{NbB}_3\text{O}_{12}$ were grown using the flux method. The crystal structure characterisation was completed using the SMART APEX II single crystal diffractometer; orthorhombic space group $\text{Pbnm}(62)$ with $a = 9.3336(7)$, $b = 9.4039(7)$ Å, $c = 3.1793(2)$ Å, $V = 279.05(3)$, $Z = 8$. The structure was solved by direct methods using the SHELXS program. The structure refinement was carried out by least-square minimization in SHELXL program using anisotropic thermal parameters of all atoms. The final indexes are $R1 = 0.0309$, $wR2 = 0.0715$, Goodness-of-fit on $F^2 = 1.051$. The dc magnetisation and heat capacity experiments were performed. The results are prepared for the publication.
- [41] M. Angst, P. Khalifah, R.P. Hermann, H.J. Xiang, M.-H. Whangbo, V. Varadarajan, J.W. Brill, B.C. Sales, D. Mandrus, Charge order superstructure with integer iron valence in Fe_2OBO_3 , Phys. Rev. Lett. 99 (2007) 086403, <https://doi.org/10.1103/PhysRevLett.99.086403>.